Bromine-adsorption-induced change in the electronic and magnetic properties of nanographite network systems

Kazuyuki Takai,* Hokuto Kumagai, Hirohiko Sato, and Toshiaki Enoki
Department of Chemistry, Tokyo Institute of Technology, Ookayama, Meguro, Tokyo, 152-8551, Japan
(Received 25 August 2005; revised manuscript received 11 November 2005; published 30 January 2006)

Nanographite having open edges has a nonbonding π-electron state of edge origin (edge state), which causes unconventional electronic and magnetic features. Bromine-adsorption effect on the electronic and magnetic properties of nanoporus carbon consisting of a flexible three-dimensional random nanographite network system is investigated by using activated carbon fibers (ACFs) as host material. The irreversible adsorption of bromine into ACFs at room temperature gives compositions up to Br/C=0.43. The interaction between nanographite and the adsorbed bromine is classified into three groups; charge transfer, covalent bonding, and physisorption interactions, where the latter two are the majorities. Although the charge transfer rate from carbon to bromine is considerably small (0.0004 per C atom at maximum), in comparison with that in bulk graphite-bromine intercalation compounds, the downshift of the Fermi energy results in the large reduction of the localized spin concentration of edge state and the orbital diamagnetism. This proves the important role of the edge state in the charge transfer process. The electron spin resonance results demonstrate the contribution of the orbital character of bromine to the edge state in nanographite through orbital mixing. The physisorbed bromine accommodated into the nanopores induces the dielectric and structural effects on the nanographite. The former causes the modification of the carrier conduction process due to the charging effect, while the latter results in the magnetic switching phenomenon induced by the effective pressure of physisorbed bromine species to the edge-state spins.

DOI: 10.1103/PhysRevB.73.035435 PACS number(s): 73.22.−f, 75.75.+a, 73.63.−b, 81.07.−b

I. INTRODUCTION

Nanosized systems have attracted great interests of physicists and chemists due to their novel electronic properties accompanied with quantum size effect, surface effect, charging effect, etc.[1,2] Especially, nanosized carbon-based materials having π-electron have been intensively investigated in the fundamental science and applications among these.[3] In the carbon-based π-electron nanosystems, typical materials such as fullerenes and carbon nanotubes are known as "closed" π-electron networks with no edges or with edges playing a minor role.[3] In contrast, nanographite characterized with a stack of nanosized graphene (nanographene) layers (hexagonal π-electron planar network) is another type of nanosized π-electron system having "open" edges. In the open-edge π-electron systems, the edges around their peripheries produce peculiar electronic features associated with the topological origin, in entire contrast to the closed π-electron systems. The circumference of an arbitrary shaped nanographene sheet is described in terms of a combination of two kinds of edges; "zigzag" edge with trans-polyacetylene type structure and "armchair" edge with cis-polyacetylene type structure. According to Fujita's theoretical calculations on ribbon-shaped nanographene sheets, the zigzag edge causes the nonbonding π-state (edge state) superimposed on the π- and π^*-bands around the Fermi level.[4–6] The edge state spatially localized around the peripheral region of zigzag edge is strongly spin-polarized, and it gives nanomagnetic features of the localized spins. On the other hand, the armchair edge generates no such novel electronic structure. The presence of edge state makes the electronic structure of nanographite essentially different from that of diamagnetic bulk graphite.

Among the examples of nanographite, activated carbon fibers (ACFs) provide an important model system from experimental aspects.[7–15] The structure of ACFs is characterized as a disordered three-dimensional (3D) network of nanographites, where each nanographite domain consists of a loose stacking of 3 to 4 nanographene layers with the mean in-plane size of 2 to 3 nm. There exists nanosized interstitial space called "nanopore" between nanographite domains.[16,17] The presence of the nanopores in ACFs results in the accommodation of a large amount of various kinds of guest molecules, where the interaction between the adsorbed molecules and the nanographites plays an important role in modifying the physical properties of the nanographite network. The interaction of the guest species with the nanographite network has three different types. The first one is generated by simple physisorption of guest molecules into the nanopores. The adsorbed molecules, which work to produce effective pressure on nanographite domains, can modify the structure of the nanographite network due to its flexible structure. Indeed, nanographite can be easily compressed along the interlayer direction by the guest molecules accommodated into the nanopore because the interlayer distance of nanographite ($\sim$0.38 nm)[18] is considerably larger than that of bulk graphite ($\sim$0.335 nm). In connection with the structural flexibility, previous works demonstrate that the water-physisorbed ACFs show a magnetic switching phenomenon in spite of the nonmagnetic nature of the water molecule, where the effective pressure of water molecules squeezes the nanographite domains, resulting in a stepwise reduction in the interlayer distance and the subsequent decrease of localized magnetic moments of the edge states as the water vapor pressure increases.[19] This is attributed to the enhancement in

the antiferromagnetic exchange interaction of the edge-state localized spins between the adjacent nanographene layers in a nanographite domain, where the effective pressure of adsorbed water molecules induces the enhancement through the compression of nanographite,[20] which works to increase the wave function overlap between the adjacent nanographene layers. The second one is the charge transfer interaction between guest and nanographite. Guest molecules having an electron donating or accepting nature induce charge transfer from them to the host nanographite, or from the host to them, respectively. In the iodine-doped ACFs, the charge transfer from nanographite to the iodine molecule lowers the Fermi level, resulting in the reduction of the orbital diamagnetism contribution.[12] The last one is related to covalent bond formation between the guest molecule and the carbon atom of nanographite, which takes place when chemically active guest species are employed. Actually, in the fluorinated ACFs systems, the introduced fluorine atom is chemically bonded to the carbon atom of ACFs, and destroys the π-electron conjugate network, resulting in the drastic changes in the electronic structure of nanographite.[14,21]

For examining these three types of host-guest interactions, the molecules in the family of halogens are useful guest species, where chemical activities vary in the wide range. Actually, iodine can induce only weak charge transfer, whereas strong covalent bonding is produced in a fluorine-nanographite system, as explained above. From this aspect, bromine, which has chemical activities intermediate between iodine and fluorine, is an interesting guest species which is expected to play multilateral roles in the host-guest interaction. In fact, its electronegativity stronger than iodine is expected to induce the charge-doping effect importantly modifying the electronic structure of the host system. The moderate chemical activity is expected to make bromine participate also in the physisorption phenomenon, in contrast to strong reactivity of fluorine which forms only covalent bonding with nanographite. The liquid nature of bromine at room temperature is a good advantage to make a large condensation of guest species in the nanopores of ACFs, which enables us to generate effective pressure acting on nanographite.

In this study, the structure, and electronic and magnetic properties of the nanographite in ACFs, which are modified by the bromine-nanographite interaction, are investigated by means of adsorption isotherm, thermogravimetry (TG), thermal desorption spectroscopy (TDS), Raman spectroscopy, electrical conductivity, magnetic susceptibility, and electron spin resonance (ESR).

II. EXPERIMENT

Commercially available pristine ACFs (Kuraray Chemicals, FR-20) were evacuated to 1×10^{-6} Torr at 200 °C in order to eliminate the adsorbed species accommodated in the nanopores and then vacuum-sealed in a Pyrex glass tube. Bromine was purified by the freeze-pump-thaw method prior to the adsorption process. Raman spectroscopy, ESR, and room-temperature electrical conductivity measurements were carried out during *in situ* bromine adsorption, while measurements of thermogravimetry (TG), mass spectroscopy (MS), temperature dependence of conductivity, and magnetic susceptibility were performed for the samples to which fixed contents of bromine were adsorbed.

The adsorption isotherm of bromine for ACFs was measured by the weight uptake method at room temperature using about 1 g of the ACFs sample. TG traces were investigated by the MacScience TG-DTA spectroscopy system in the temperature range up to 1000 °C at an argon gas flow rate of 100ml/s, and a temperature elevation rate of 100 °C/min. TDS spectra were measured by a Spectra Microvision quadrapole-type mass spectrometer in the temperature range up to 800 °C with a temperature elevation rate of 10 °C/min. Raman spectroscopy measurements were performed using Jobin-Yvon T64000 instruments with an argon-ion laser operated at 514.5 nm with an output power in the range of 10–30 mW in the backscattering geometry.

dc electrical conductivity measurements were performed for a single fiber along its fiber axis in the temperature range from 4.2 K to room temperature. Because of the high resistance of the samples, a two contacts method was adopted for all of the measurements. Prior to the measurement, the samples were electrically contacted to gold wires with carbon paste and vacuum sealed in a glass cell. Magnetic susceptibility measurements were carried out by a superconducting quantum interference device magnetometer (Quantum Design MPMS5) in the field of 1 T between 2 and 380 K, where about 20 mg of the samples vacuum-sealed in quartz tubes were used. At 2 and 300 K, magnetization measurements were also performed in the field up to 5.5 T. ESR spectra were measured with a conventional ESR *X*-band spectrometer (JEOL JES-TE200) at room temperature for typically 1 mg samples sealed in a quartz sample tube. In order to prevent the surface skin depth effect, the fabric axes of bundled fibers were oriented perpendicular to the electric field direction of the microwave.

III. RESULTS

Figure 1 shows the bromine adsorption isotherm at 298 K with respect to relative bromine pressure p/p_0 (p_0=33.3 kPa: saturated vapor pressure at 298 K). Hereafter, the bromine contents of the nonadsorbed ACFs and the bromine-adsorbed ACFs (Br-ACFs) are represented by the atomic ratio of bromine to carbon (Br/C). The adsorption isotherm is irreversible with a large hysteresis between the adsorption and desorption processes. In the initial adsorption process for the virgin sample, the atomic composition ratio for Br-ACFs shows a steep increase in the low pressure region ($p/p_0<0.1$) and reaches almost saturated value Br/C=0.43 corresponding to 2.9 g of Br for 1 g of ACFs at $p/p_0\approx0.5$. In the desorption process, the adsorbed bromine is hardly removed even in vacuum, and reaches a finite value Br/C=0.27 corresponding to 1.8 g for 1 g of ACFs at $p/p_0\approx0.001$. In the general cases of physisorption into nanoporous systems, the hysteretic isotherms appear because of the difference in the curvatures of meniscus of adsorbed liquid in the pore between the adsorption and desorption processes.[22] However, the extremely large hysteresis behav-

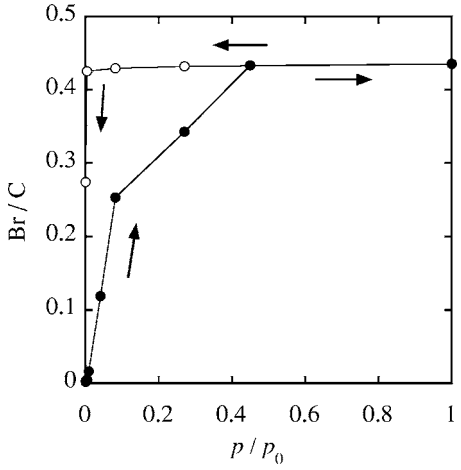

FIG. 1. The bromine adsorption isotherm for ACFs at 298 K. p_0 are the saturated vapor pressure (33.3 kPa) at 298 K. Closed circles and open circles denote the adsorption process for the virgin sample, and the subsequent desorption process, respectively. The arrows indicate the sequence of the process.

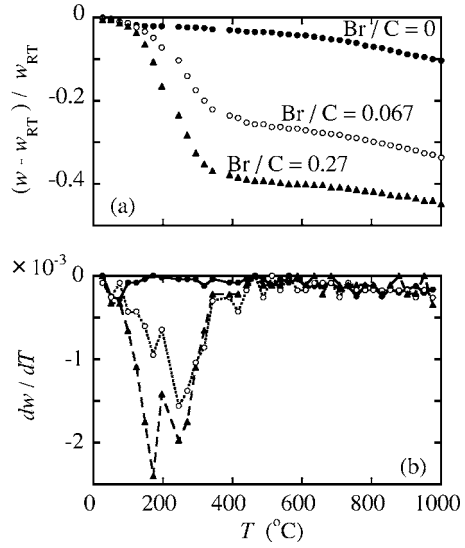

FIG. 2. TG traces for nonadsorbed ACFs (closed circles), Br/C=0.27 (closed triangles), and Br/C=0.067 (open circles). Scan rate is 100 °C/min. (a) w vs T plot. (b) dw/dT vs T plot. Weight change w in the vertical axis is normalized with the initial weight at room temperature $w_{RT}=1$.

ior in the present experiment is beyond the feature of the physisorption process, where the adsorbed bromine remains still accommodated in ACFs even under enough low pressure condition ($p/p_0 \approx 0.001$). This suggests the irreversible adsorption/desorption feature associated with chemical reaction. The observed steep increase in the initial stage of the adsorption process for the virgin sample also suggests the feature of chemisorption, which does not appear in the isotherm for chemically inert nitrogen gas.[23] The volume of the nanopore is estimated as 0.75 cm^3 (g of ACFs)$^{-1}$ for the ACFs sample (FR-20).[24,25] On the other hand, with the density of bulk liquid bromine $d_{Br}=3.12$ g cm^{-3} at 293 K, the volume of adsorbed bromine in 1 g of ACFs is calculated as 0.89 and 0.58 cm^3 (g of ACFs)$^{-1}$ for Br/C=0.43 and 0.27, respectively. Taking the structural flexibility of nanographite into consideration, the excess amount of adsorbed bromine molecules [0.9 cm^3 (g of ACFs)$^{-1}$] beyond the volume of the nanopores [0.75 cm^3 (g of ACFs)$^{-1}$] for Br/C=0.43 is attributed to the expansion of the nanopores accompanied with the shrinkage in the interlayer distance of nanographite and/or the presence of chemisorption species adsorbed at the edge sites of nanographite. It should be noted that the saturated value for the volume of adsorbed molecules with similar calculation is estimated as 0.75 and 0.70 cm^3 (g of ACFs)$^{-1}$ for nitrogen and water, respectively.[19,23] In the nitrogen and water adsorption cases, the squeezing effect on the nanographite by the excess amount of the molecules adsorbed in the nanopore is confirmed by the electron transport, ESR, and x-ray diffraction studies.[10,18,19] The large adsorbed amount in the bromine case suggests that guest molecules are not only simply physisorbed without any extra changes but also chemisorbed with changes in the electronic structure of nanographite.

The TG traces and their derivatives with respect to the temperature are shown in Figs. 2(a) and 2(b), respectively, for the nonadsorbed ACFs (Br/C=0) and Br-ACFs with Br/C=0.27 and 0.067. For the nonadsorbed ACFs, a slight weight change ω (ca. −2%) is observed in the initial stage of the heating process below 100 °C, which is followed by a slight monotonical declination of the weight up to the highest temperature investigated (1000 °C). The initial weight change is caused by the desorption of adsorbed gaseous species coming from ambient atmosphere, while the dissociation of functional groups attached to the peripheries of nanographite domains is responsible for the change at the high temperatures. Br-ACFs with Br/C=0.27 and 0.067 show a steep decrease around 150–250 °C in addition to the ACFs-inherited desorption below 100 °C of adsorbed ambient gases. This decrease is responsible for peaks appearing at 170 and 250 °C in the dw/dT vs T curves in Fig. 2(b). A peak appears also around 410 °C in Fig. 2(b) for Br-ACFs with Br/C=0.27 and 0.067. The weight losses calculated based on the sample composition with an assumption of complete desorption of bromine are 68% and 38% for Br/C=0.27 and 0.067, respectively, where the contribution of the adsorbed ambient gases and the dissociation of functional groups (~10%) observed in the TG trace for the nonadsorbed ACFs are included. The observed weight losses for Br/C=0.27 and 0.067 at 1000 °C are obtained as 45% and 34%, respectively. Therefore there is a large discrepancy between the experimental and calculated results in Br/C=0.27, although the calculated value is in good agreement with that experimentally observed in the sample with Br/C=0.067. This suggests the presence of bromine species, which cannot be removed even around 1000 °C, in the prolonged reaction duration with the higher vapor pressure of bromine. In other words, a part of bromine atoms are bonded covalently to the carbon atoms of aromatic rings with the extreme stability against pyrolysis. This is reminiscent of the stability of halogenated aromatic compounds such as PCB (polychlorinated biphenyls).[26] The difference between the experimental and calculated weight losses therefore indicates

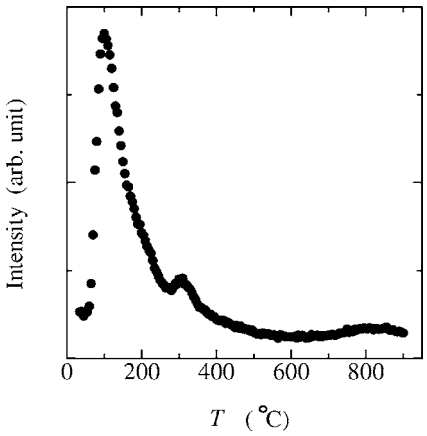

FIG. 3. Temperature dependence of the mass fragment peak intensity integrated in the mass number range between 79 and 82, which are assigned to bromine atom and HBr species, for Br/C=0.27 with a heating rate of 10 °C/min.

that ca. 35% of the adsorbed bromine remains as well-stabilized covalent species around 1000 °C for the sample with Br/C=0.27. In the sample with Br/C=0.067, the lower vapor pressure in the adsorption process causes a lesser contribution of the extremely stable components in the covalently bonded species.

Thermal desorption spectroscopy (TDS) provides more detailed information on the adsorption state of bromine in ACFs. Figure 3 shows the temperature dependence of the mass fragment peak intensity integrated within the mass numbers between 79 and 82, which are assigned to bromine atom and its derivatives such as ^{79}Br, H^{79}Br, ^{81}Br, H^{81}Br, with a heating rate of 10 °C/min for the Br-ACFs (Br/C=0.27). The mass fragment intensity is peaked at four temperatures 100, 170, 300, and 800 °C, which suggests the presence of four desorption sites having different binding energies. The strong peak at 100 °C accompanied with a shoulder around 170 °C comes from physisorbed bromine species. This peak and the shoulder correspond to the steep drop at 170 °C in the derivative of TG trace at a rapid scan rate of 100 °C/min, where the shoulder peak in the TDS spectrum is completely merged into the main peak. Comparison of the TG traces and the TDS spectra at the different scan rates gives an estimate of an adsorption enthalpy of 38 kJ/mol on the basis of assumption of the first-order desorption process. The observed adsorption enthalpy is comparatively larger than that of ordinary physisorption ranging below 30 kJ/mol, suggesting that the physisorbed bromine species are well-stabilized through trapping by the enhanced potential of nanographite walls.[27] This is responsible for the sticky nature of physisorbed bromine even in vacuum.

A peak around 300 °C corresponds to the small peak in the TG trace around 410 °C at a rapid scan rate of 100 °C/min, giving an adsorption enthalpy of 62 kJ/mol, which is in the energy range intermediate between chemisorption and physisorption. Taking into account that regular graphite forms graphite intercalation compounds through charge transfer from graphite to bromine with an enthalpy change of 45.6 kJ/mol,[28] we can consider that the peak at 300 °C is the consequence of charge transfer (CT) interaction. The highest temperature peak (800 °C), which is in the same energy range as the bond breaking energy for the bromine of bromobenzene (e.g., 333 kJ/mol),[29] is attributed to the bromine covalently bonded to carbon atoms of nanographites. The peak around 800 °C consists of only the species with the mass number 80 (H^{79}Br), 82 (H^{81}Br) in contrast to the lower temperature peaks. From the chemical point of view, the desorption process of the bromine atom covalently bonded with the edge carbon atoms of an aromatic conjugated system is usually accompanied with the formation of HBr.[30] Moreover, considering the findings that the edges are more chemically active than the interior in the nanographite of ACFs,[14] covalently bonded bromine is expected to be not bonded with the interior carbon atom of nanographite but with the edge carbon atoms. This is evidenced by the Raman spectroscopy results as will be shown later.

The peak intensity ratio for Br/C=0.27, where the shoulder is involved in the peak at 100 °C, is estimated as 7:2:1 for the peaks at 100, 300, and 800 °C. The populations of the physisorbed, the CT, and covalent bromine species can be estimated from the intensity ratio of the three peaks in the TDS spectra, after the correction for the contribution of covalent bromine species (ca. 35%) that are stable even around 1000 °C is made. Then, the corrected populations (Br_{CT}:Br_{CB}:Br_{AD}) are estimated as ca. 13:42:45 for the ratio of the CT, the covalent, and the physisorbed bromine species for Br/C=0.27. Therefore the majority of bromine adsorbed in the nanopore of ACFs is assigned to the physisorbed species accommodated into the nanopore between nanographites, the second majority is covalently bonded bromine, and the CT species are the minority.

Let us find the correlation between the amount of the CT bromine species and the structure of nanographite. The estimated population of the CT species corresponds to the ratio of $Br_{CT}/C=0.035(=0.13\times0.27)$ for the sample of Br/C=0.27. From the density of bulk liquid bromine, the effective radius is estimated as 0.185nm for one adsorbed bromine atom with spherical approximation. As the individual nanographite domain in ACFs is formed with the stack of ca. 3 graphene layers with the mean in-plane size of 2.5 nm, the bromine content necessary for completely covering the nanographite surface in ACFs is calculated as $Br_{CT}/C=0.07$ on the assumption that the monolayers of bromine are placed on the two graphitic surfaces of the domain at the same density as that of bulk liquid and the nanographite is circular shaped with a diameter of 2.5 nm.

This is in good semiquantitative agreement with the experimental results of the content (0.035) of bromine with CT-interaction. Therefore, among bromine species accommodated in the nanopore, only those directly faced to nanographite surfaces are subjected to form weak CT bonding with nanographite.

The Raman spectra for Br-ACFs exhibit peaks assigned to graphite structure in the high frequency region ($1300-1700\ cm^{-1}$)), while the peaks for the stretching mode of bromine molecule is observed in the low frequency region ($300-700\ cm^{-1}$)) especially for the sample with an excess bromine vapor in the sample cell (Br/C=0.43). The ob-

served peaks in the low frequency region are not attributed to the intrinsic vibration modes for adsorbed bromine molecules in ACFs because the bromine stretching mode is associated with the bromine gas in the sample cell. Similar as typical disordered graphite systems, the Raman spectra for Br-ACFs in the high frequency region are composed of two broad peaks around 1360 and 1590 cm^{-1}, which are assigned to the *D*-band peak and *G*-band peak in the general first-order features, respectively.[31] For all of Br-ACFs, the position of the *D*-band peak and the relative intensities of both peaks are almost invariable irrespective of the composition ratio, while the *G*-band peak positioned at 1590 cm^{-1} for the nonadsorbed ACFs is shifted up to 1597 cm^{-1} for Br-ACFs (Br/C=0.27), as the bromine content increases. Because the G/D peak intensity ratio is correlated to the range of the in-plane graphitic structural coherence, for estimating the in-plane size, we can employ the empirical relation between the in-plane size of the graphitic domain and the G/D peak intensity ratio obtained for various disordered graphitic materials; $L_a = 4.4 \times (\text{Intensity})_{(G\ \text{band})}/(\text{Intensity})_{(D\ \text{band})}/\text{nm}$.[32] In-plane size L_a of graphitic domain estimated from the relation is about 2.2 nm for Br-ACFs, which is independent of the bromine content. The invariability of L_a on the bromine content indicates that the in-plane structure of nanographite is conserved during the bromine-adsorption process. The adsorbed bromine and the carbon atom located in the interior of nanographite plane are not coupled by strong bonding, which otherwise contributes to fractionalizing the extended graphitic π-electron network. Namely, the covalently bonded bromine suggested in the TG and TDS results is associated with the covalent bond formation of bromine atom with the carbon atoms at the edges of nanographite domains.

For the covalently bonded bromine species, there are two types of bonding structures. One is the bonding produced by the substitution of the functional groups of the nanographite edges with bromine, while the other is that produced by the addition of bromine to the edge carbon atoms with the edge functional group or bromine having been bonded. The latter reduces the conjugated π-electron system since the addition reaction destroys the hexagonal aromatic rings at the edges. According to the Raman experiments, the size of the π-electron system is not reduced upon the bromine uptake. Therefore the substitution reaction at the edge is mainly responsible for the formation of the covalent-bonded bromine species. The presence of the bromine species, which can remain in the pyrolysis around 1000 °C, is consistent with the major role of the substitution reaction. From this consideration, the maximum amount of the covalent-bonded species is estimated as $Br_{CB}/C = 0.17$ on the assumption that all the edge carbon atoms of a circle-shaped nanographene with a diameter of 2.5 nm are monobrominated. The experimentally obtained amount $Br_{CB}/C = 0.11 (= 0.42 \times 0.27)$ is ca. 65% of that calculated. Eventually, it is suggested that the circumference of nanographene sheets are mostly terminated by the covalent bromine species.

The peak position of the *G*-band (k/cm^{-1}) is related to the position of the Fermi energy of graphite, where the CT rate f_c per carbon atom from graphite to guest species is described by the empirical formula;[33,34]

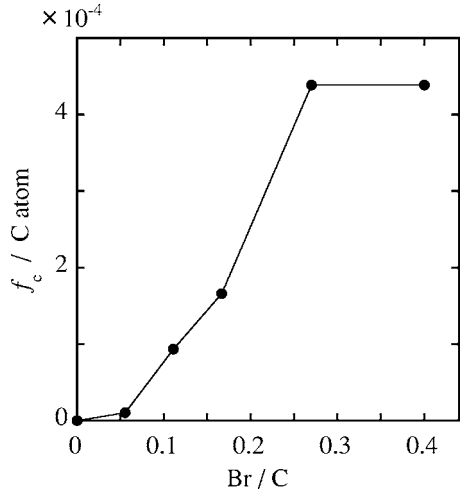

FIG. 4. CT rate f_c per carbon atom for Br-ACFs as a function of bromine content.

$$-1.63 \times 10^{-6}(k-1590)^2 = 0.157 f_c + 0.146 f_c^{3/2} + 0.236 f_c^2.$$

CT rates f_c for Br-ACFs at various bromine contents are shown in Fig. 4 after being calculated with the formula. As the bromine content increases, f_c steeply increases in the region of $Br/C < 0.27$, and reaches almost a saturated value $f_c = 0.0004$ for $Br/C > 0.27$. The saturated value at Br/C=0.27 is about one order of magnitude smaller than that of bulk graphite intercalation compounds ($f_c \sim 0.002$).[35] This fact suggests that bromine is not well intercalated in the galleries between graphene layers in individual nanographitic domains, being consistent with the results obtained by TG and TDS that most of the bromine species are accommodated physisorptively in the nanopores or covalently bonded to the carbon atom of nanographite, while only bromine species directly faced to the graphene surfaces are subjected to the CT with nanographite. This is also favorable for the fact that CT takes place only between guest species and a graphene layer being faced to each other in the higher stage graphite intercalated compounds.[34]

Figure 5(a) shows the bromine content dependence of the conductivity for Br-ACFs at room temperature. As the bromine content increases, the electrical conductivity rapidly increases in the low bromine content region ($0 < Br/C < 0.2$), and becomes almost saturated above 0.2, where the saturation value is estimated as $\sigma/\sigma_0 \sim 4$ (σ_0: the conductivity of the nonadsorbed ACFs). Figure 5(b) shows the time dependence of the conductivity for Br-ACFs (Br/C=0.43) at room temperature during the evacuation process. When the sample is evacuated by liquid nitrogen trap at $t=0$, the conductivity starts decreasing rapidly, and it becomes almost constant in 10 min, where the value in the steady state is $\sigma/\sigma_0 \sim 2.4$ even in the long duration of evacuation. This is consistent with the results of the adsorption isotherm shown in Fig. 1. Indeed, the fact that the steady state conductivity is larger than the conductivity before bromine adsorption suggests that the bromine species remain in the interior of ACFs even in vacuum.

The temperature dependence of the conductivity for the nonadsorbed ACFs and Br-ACFs (Br/C=0.27) is shown in Figs. 6(a) and 6(b). The temperature dependence of the con-

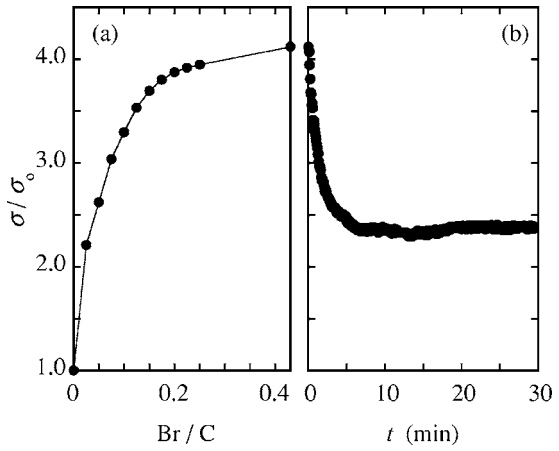

FIG. 5. (a) The bromine content dependence of the electrical conductivity for Br-ACFs at room temperature. (b) The time dependence of the conductivity in the bromine desorption process for the Br-ACFs (Br/C=0.43) at room temperature. The conductivity is normalized with respect to that for the nonadsorbed ACFs σ_0.

ductivity σ for the nonadsorbed ACFs and Br-ACFs (Br/C=0.27) obeys the $\ln \sigma$ versus $T^{-1/2}$ law, and the $\ln \sigma$ versus $T^{-1/4}$ law, respectively. In the case of the nonadsorbed ACFs, the linear relation between the $\log \sigma$ and $T^{-1/2}$ indicates that the carrier conduction process is dominated by Coulomb gap variable range hopping (CGVRH) in Anderson insulator, taking into account the three-dimensionality of the nanographite network. In the CGVRH conduction process, the temperature dependence of the conductivity is described by

$$\sigma = \sigma_\infty \exp\left[-\left(\frac{T_0}{T}\right)^{1/2}\right], \quad T_0 = \frac{6e^2}{\pi k_B} \frac{1}{4\pi\epsilon_r\epsilon_0} \frac{1}{\xi}, \qquad (1)$$

where σ_∞, ϵ_r, ϵ_0, and ξ are the conductivity at $T=\infty$, the relative dielectric constant representing the screening effects on the charge at metallic islands, the permittivity of vacuum, and the localization length of the wave function, respectively.[36]

In contrast, the linear relation in the $\log \sigma$ vs $T^{-1/4}$ plot for Br-ACFs (Br/C=0.27), which is characteristic of 3D variable range hopping, demonstrates that the charging effect becomes less important in the electron hopping process in the case of Br-ACFs. According to the CGVRH conduction model,[36] the characteristic temperature, below which the charging effect is effective in the conduction process, is described as

$$T_c = \frac{e^4 D(E_F)}{(\epsilon_r \epsilon_0)^2} \xi, \qquad (2)$$

where $D(E_F)$ is the density of states at the Fermi level. The difference in the temperature dependence of the conductivity between the nonadsorbed ACFs and Br-ACFs is considered to be the change in T_c in the conduction mechanism at low temperatures. Namely, the temperature range investigated is lower than T_c for the nonadsorbed ACFs, whereas it is higher than that for Br-ACFs.

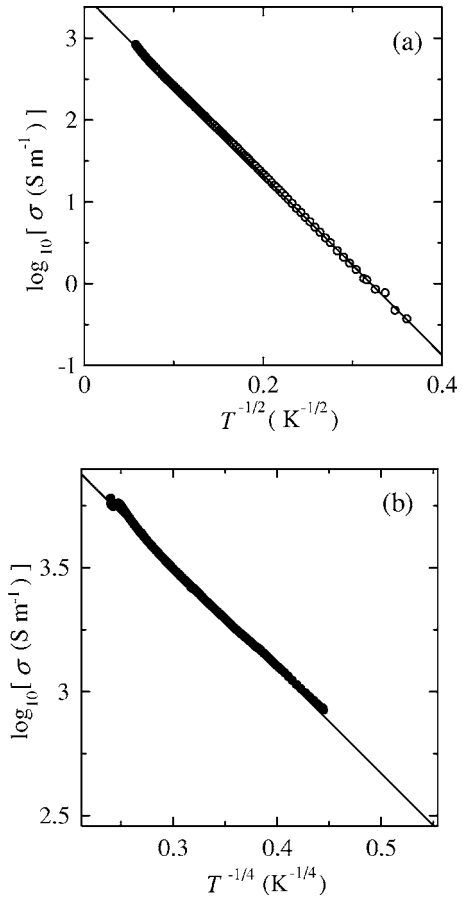

FIG. 6. The temperature dependence of the conductivity σ for (a) the nonadsorbed ACFs obeying $\ln \sigma$ vs $T^{-1/2}$ law (solid line) and (b) Br-ACFs with Br/C=0.27 obeying the $\ln \sigma$ vs $T^{-1/4}$ law (solid line).

In the nonadsorbed ACFs, the susceptibility is described with a combination of a Curie-Weiss term χ_c and a temperature-independent term χ_0, as represented by the following equation:

$$\chi = \chi_c + \chi_0 = \frac{C}{T - \Theta} + \chi_0, \qquad (3)$$

where C and Θ are the Curie constant and the Weiss temperature, respectively. For Br-ACFs, as will be discussed later, the spin magnetism given by χ_c is affected mechanically by the physisorbed bromine in the higher temperature region, although the observed susceptibility obeys Eq. (3). Thus χ_0 is obtained by fitting the susceptibility to Eq. (3) in the temperature range of 100–200 K, in which the physisorbed bromine freezes. Figure 7 shows the reciprocal susceptibility χ_c^{-1} versus T plots for Br-ACFs ($0 \leqslant$ Br/C $\leqslant 0.27$). As seen in the figure, the deviations from the linearity in the χ_c^{-1} versus T plots are observed at high temperature for the bromine-adsorbed samples, where the deviation is enhanced with the increase in bromine content. The gradients of the χ_c^{-1} versus T plots for Br-ACFs are changed around 80 and 230 K as schematically shown by the inset of Fig. 7, which suggests the presence of three temperature regions;

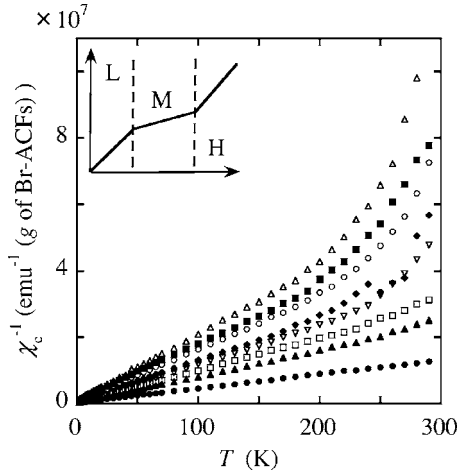

FIG. 7. χ_c^{-1} vs T plots for Br-ACFs ($0 \leqslant Br/C \leqslant 0.27$). ●, □, ▲, ▽, ◆, ○, ■, and △ denote the data for the nonadsorbed ACFs and Br-ACFs with Br/C=0.038, 0.067, 0.083, 0.10, 0.14, 0.16, and 0.27, respectively. The inset shows schematically three divided temperature regions (L, M, H), which are obtained based on the difference in the susceptibility behavior.

"L" ($T \lessapprox 80$ K), "M" ($80 \lessapprox T \lessapprox 230$ K), and "H" ($T \lessapprox 230$ K). This appears more clearly in the $\chi_c T$ vs T plots shown in Fig. 8(a). In the temperature regions H and L, the values of $\chi_c T$ strongly depend on the temperature. This suggests that the conventional analysis with the χ_c^{-1} vs T plot is valid only in the region M for obtaining the value of the Curie constant. In addition, the decreasing trends in the value of $\chi_c T$ in the regions L and H are suggestive of the reduction in the magnetic moments associated with antiferromagnetic spin fluctuations.

The observed localized spins from the Curie-Weiss term are considered to have $S=1/2$, judging from the behavior of the magnetizations. The bromine content dependence of the localized spin concentration N_s obtained from the Curie constant is shown in Fig. 9 for the intermediate region M. The spin concentration rapidly decreases with the increase in the bromine content in the early stage of bromine adsorption up to ca. Br/C ~ 0.05, while the decrease becomes moderate above that bromine content.

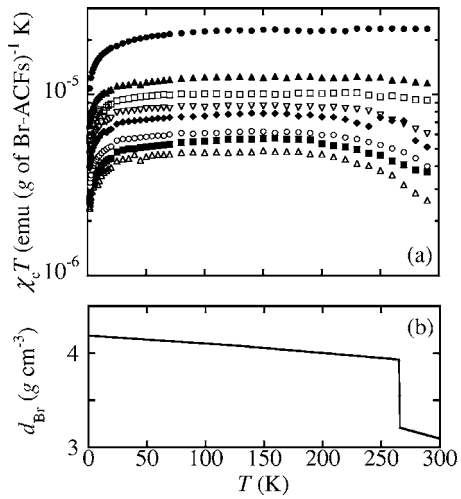

FIG. 8. (a) $\chi_c T$ vs T plots for Br-ACFs ($0 \leqslant Br/C \leqslant 0.27$). ●, □, ▲, ▽, ◆, ○, ■, and △ denote the data for the nonadsorbed ACFs and Br-ACFs with Br/C=0.038, 0.067, 0.083, 0.10, 0.14, 0.16, and 0.27, respectively. (b) The temperature dependence of the mass density of bulk bromine (Refs. 40 and 41).

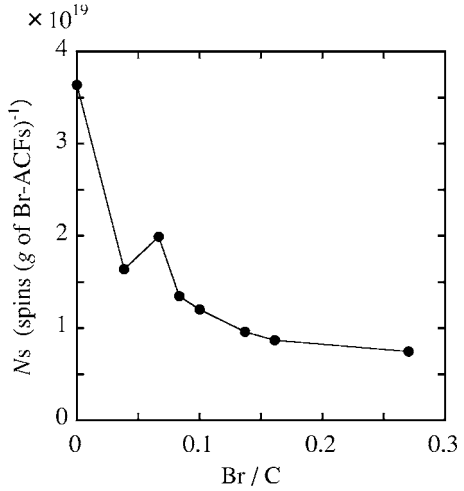

FIG. 9. The bromine content dependence of the localized spin concentration N_s. The solid lines are the guide for the eyes.

Temperature-independent term χ_0 consists of mainly the core diamagnetism and the orbital magnetism χ_{orb} of the π-electron on the graphitic plane, where the Pauli susceptibility is more than one order of magnitude smaller than the orbital susceptibility in the graphitic system.[15]

Figure 10 shows the bromine content dependence of the orbital susceptibility, which is obtained by subtracting the contribution of the Pascal core diamagnetism from the observed value of χ_0. Taking into account that the observed orbital susceptibility is directionally averaged in the 3D nan-

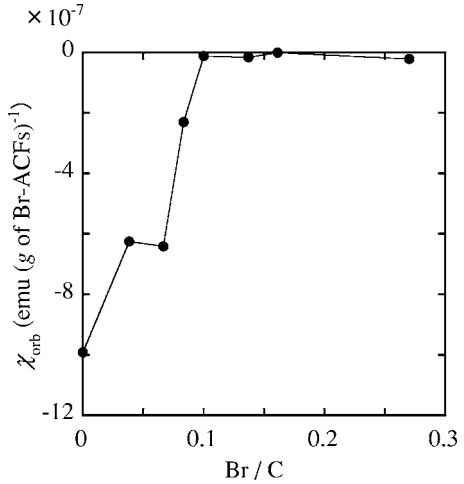

FIG. 10. The bromine content dependence of the orbital susceptibility χ_{orb} in the field perpendicular to the graphitic plane. The value of χ_{orb} is obtained by multiplying the observed temperature independent term χ_0 by 3 after the subtraction of the Pascal diamagnetic susceptibility. The value of χ_0 has ambiguity of less than 10% due to the contribution of the Pauli paramagnetism. The solid line is the guide for the eyes.

ographite network of ACFs, the in-plane orbital susceptibility χ_{orb} is obtained after multiplied by 3. χ_{orb} is diamagnetic and increases steeply in the initial stage of bromine adsorption upon the increase of bromine content up to ca. $Br/C \sim 0.1$, above which χ_{orb} becomes negligible.

The magnetizations are less than those expected from the Brillouin curve for noninteracting spins with $S=1/2$ at low temperatures for all the Br-ACFs with the various bromine contents, suggesting the presence of antiferromagnetic interaction.

The ESR signal of Br-ACFs appears as a broad single Lorentzian peak at room temperature in the range of $0 \leqslant Br/C \leqslant 0.23$. On the other hand, the signal is not observable for $Br/C > 0.23$ because of a considerable reduction in the Q-value of the microwave cavity associated with the increase in the conductivity upon bromine adsorption, in addition to the broadening of the signal. In the nonadsorbed ACFs, the Lorentzian line shape suggests the homogeneity of the spin system, in which the exchange narrowing mechanism is at work between the localized spins. This is consistent with the feature of edge-state spins, since the π-conduction electron can mediate interactions between the localized spins. The observed localized spin concentration $\sim 6 \times 10^{19}$ spins g^{-1} for the nonadsorbed ACFs gives an estimate of the dipolar width less than 0.1mT, if the spins are homogeneously distributed in space. The estimated width is an order of magnitude smaller than the observed linewidth of 6.2 mT. This implies an inhomogeneous spatial distribution of the localized spins, which can be understood on the basis of the hierarchical structural feature of ACFs. Actually, the ACF structure consists of a 3D network of nanographite domains, each of which is formed by the stacking of 3 to 4 nanographene layers. An edge-state spin on a layer interacts with another spin on an adjacent layer in the same nanographite domain, in which the distance between the two spins is considerably shorter than the mean spin-spin distance. The antiferromagnetically coupled spins between adjacent layers give an effective magnetic moment on a nanographite domain, which interacts weakly with that on the adjacent nanographite domain. Thus the interplay between the dipolar interaction and the exchange interaction in this inhomogeneous structure is responsible for the linewidth and line shape observed in the nonadsorbed ACFs. Figure 11 shows bromine content dependence of the linewidth ΔH_{pp} and g-value for Br-ACFs, at room temperature.

The linewidth ΔH_{pp} drops slightly in the initial stage of bromine adsorption. Such trend in the ESR linewidth is observed also in the oxygen adsorbed ACFs,[10] and is considered as the common effect of the chemisorbed guest species on the ACFs. As the bromine content increases, ΔH_{pp} increases linearly and it reaches about 12 mT at $Br/C=0.23$. The g-value is estimated at 2.0004 at $Br/C=0$, which is much less than that of free electron spin value $g_0=2.0023$, and it is in the same range as that of the edge-state spins observed in the nanographite prepared by heat treatment-induced graphitization of nanosized diamond.[11] It decreases with the elevation of bromine content, and it approaches 1.99 at $Br/C=0.23$.

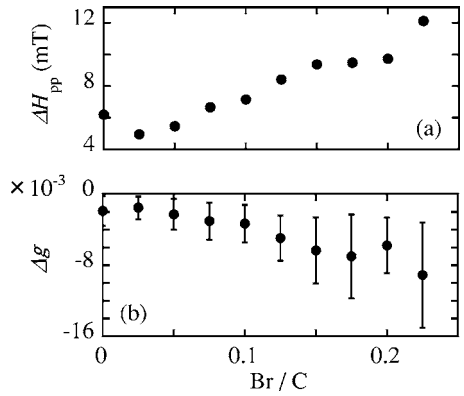

FIG. 11. The bromine content dependence of the ESR linewidth ΔH_{pp} (a) and the g-value (b) at room temperature. The g-value is denoted as the difference from that of the free electron spin ($\Delta g = g - 2.0023$).

IV. DISCUSSION

There are three types of host-guest interactions, which govern the bromine adsorption process in ACFs. Actually, the experimental findings indicate that the interactions produce the following three kinds of bromine species: (1) bromine atoms bonded to the edge carbon atoms with covalent bondings (CB), which are produced through substitution reaction, (2) bromine species subjected to the charge transfer (CT) with nanographite, where the bromine species are faced to the outer surface of nanographite domains, and (3) bromine molecules simply physisorbed (AD) in the nanopores between nanographite domains. The TG and TDS results of the Br-ACFs with $Br/C=0.27$ give information on the ratio of these species, which is given as $Br_{CT}:Br_{CB}:Br_{AD} = 13:42:45$. The interaction with the host nanographites is strongest in the covalently bonded bromine species, whereas the physisorbed bromine molecules are subjected to the weak van der Waals interaction.

The changes of the electron transport and magnetic properties upon bromine uptake into the nanographite network is the consequence of these three kinds of interactions. Here, it is worth summarizing the electronic structure of the 3D randomly networked nanographite domains in ACFs, as the starting material before bromine uptake. The electronic structure of nanographite domains, which are composed of a loose stacking of 3 to 4 nanographene layers, is governed by an individual constituent nanographene layer because of the considerably weak intergraphene-layer interaction associated with the significantly larger interlayer distance (~ 0.38 nm) than that of bulk graphite. The electronic structure of individual nanographene is featured with the edge state of nonbonding π-electrons, which is superimposed on the linear π- and π^*-bands around the Fermi energy.[12] Accordingly, the magnetism of ACFs is characterized with the localized spins of the edge state and the large orbital diamagnetism of the conjugated π-electron system delocalized on the whole area of the graphene layer. In the meantime, the hopping conduction of the carrier between the metallic nanographite domains dominates the electron transport of ACFs.[12]

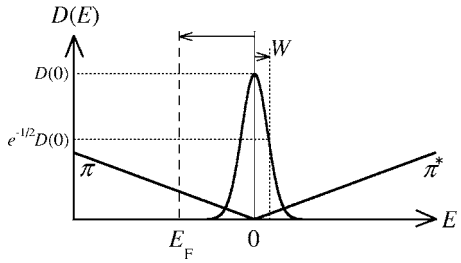

FIG. 12. The schematical band structure of actual nanographite in ACFs. π and π^* are the graphitic linear bonding and antibonding bands with the density of states $D(E)=8|E|/3\pi a^2 c\gamma_0^2$, respectively. The Gaussian function with half width W and the peak height $D(0)$ in the density of states is assumed for the edge-state band. The vertical dashed and solid lines denote the position of the Fermi energy E_F, and the degenerate point, respectively. E_F is measured by the shift from the degenerate point. Dotted lines denote the characteristic points of the electronic structure.

A. Charge transfer interaction in nanographite

The first place of the discussion is devoted to the CT bromine species, which work to shift the Fermi energy of the nanographites. Judging from the trend in the CT rate depending on the Br/C ratio, the CT bromine species are produced in the Br/C range up to 0.27 as revealed in Fig. 4. CT affects the feature of the localized spin of edge state. Actually, the localized spin concentration shown in Fig. 9 decreases in the initial stage of bromine adsorption up to Br/C$\sim$0.05 with the increase in the bromine content. These findings therefore imply that the change in the localized spin concentration is simply related to CT. The edge state of nanographite responsible for the localized spins is almost dispersionless with its density-of-states peak around the degenerate point of the π- and π^*-bands.[12] In the nonadsorbed ACFs, the Fermi energy is located around the degenerate point. The downshift of the Fermi energy in nanographite, which is induced by CT from graphite to bromine, suppresses the edge-state contribution to the electronic states around the Fermi energy, resulting in the reduction in the localized spin concentration N_s. Considering that theory predicts the flatband feature of the edge state having an extremely narrow bandwidth,[5] the localized spins are expected to disappear steeply with only a slight bromine uptake. This contradicts with the experimental finding that shows a moderate decrease of spin concentration upon the increase in the bromine content. In the case of actual nanographite in ACFs, the bandwidth of the edge state becomes broadened, as the nanographene edges are covered with various kinds of functional groups giving the perturbation potentials to the edge states. In addition to this, the boundary scattering of electrons in nanographites works as another contribution to the level broadening. Consequently, deviating from the theoretically predicted sharp peak of the edge state, the edge state of the actual nanographite has a moderately broadened peak in the density of states at the degenerate point as schematically described in Fig. 12, where, for simplicity, the density of states of the edge state is represented by a Gaussian function with half width W and peak height $D(0)\equiv D(E=0)$, while the π- and π^*-bands have linear energy dependence in the density of states.[37]

Here, we analyze the CT effect on the edge-state spins on the basis of this schematic model on the assumption that the nanographite mass density is the same as that of bulk graphite. This assumption causes an error of ca. 10% in the values of the density of states and the localized spin density. The shift of the Fermi energy E_F by CT is measured from the degenerate point (see the vertical dashed line in Fig. 12). Then, taking the number of carbon atoms per unit area of graphene into consideration, the localized spin density n_s per gram of carbon and the CT rate f_c per carbon atom are described as

$$n_s = \frac{\sqrt{3}a^2 c}{4}\frac{N_A}{M}\int_{-\infty}^{E_F} D(0)\exp\left(-\frac{E^2}{2W^2}\right)dE, \tag{4}$$

$$f_c = \frac{a^2 c}{2}\int_{E_F}^{0} D(0)\exp\left(-\frac{E^2}{2W^2}\right)dE + \frac{2E_F^2}{3\pi\gamma_0^2}, \tag{5}$$

where $\gamma_0=3.12$ eV,[31] a, c, M, and N_A are the in-plane transfer integral, the in-plane and interplane lattice constants for bulk graphite, the atomic weight of carbon, and the Avogadro's number, respectively. The first and second terms in Eq. (5) represent the contributions of the edge state, and the linear π- and π^*-bands, respectively. The trend in the observed CT rate dependence of the localized spin density n_s is expected to be explained using this electronic structure model.

Figure 13(a) shows the observed CT rate dependence of the localized spin density n_s, which is obtained from the results in Figs. 4 and 9, where the flat region M is employed since the mechanical effect of the guest bromine is absent in this temperature region as will be shown later. The experimental results are fitted to Eqs. (4) and (5) as shown with a solid line in Fig. 13(a). In the calculation, it should be noted that the spin density in the nonadsorbed ACFs uniquely determines the maximum value of f_c, above which the localized spins disappear since only the edge states are responsible for the localized spins. There is an apparent large discrepancy in the fitting between the observed and calculated f_c dependence of n_s. Indeed, in the experiment, the spin density decreases steeply as the CT rate is elevated up to $f_c\sim0.0001$, in addition to the fact that there is a CT-independent contribution, which is about 50% of the spin density in the nonadsorbed ACFs at $f_c=0$, as shown by the dashed line in the figure. In contrast, the calculated result shows a moderate and monotonical decrease. This discrepancy is associated with the too simplified model employed in the calculation. The discrepancy can be understood on the basis of the inhomogeneous charge distribution between the graphene layers as shown in Fig. 14. The nanographite domain consists of stacking of 3 to 4 nanographene layers as described before. According to the results of TG and TDS experiments, the CT bromine species are adsorbed only on the outer surface of the graphene layers faced to the nanopore, whereas the graphene layers in the interior of the domain are intact. As we know from the charge transfer feature in bulk higher stage graphite intercalation compounds, the charge transfer takes place at the graphene sheets faced to the intercalates (bounding layers), whereas the screening effect

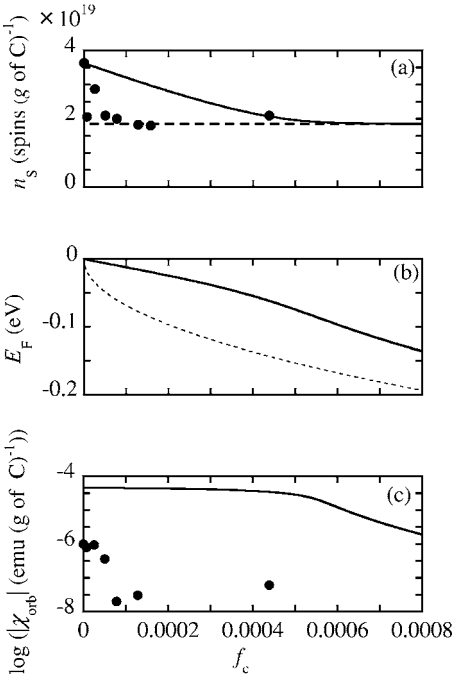

FIG. 13. The CT rate f_c dependence of (a) the localized spin density n_s per gram of carbon in the intermediate temperature range M, (b) the Fermi energy, and (c) the orbital susceptibility χ_{orb} per gram of carbon. The experimental data (full circles) in (a) and (c) are obtained after Figs. 4, 9, and 10. The horizontal dashed line in (a) is the CT-independent contribution of the localized spins. The solid curve in (a) is the fitting curve to the model shown in Fig. 12 (see text). The calculated n_s is obtained on the assumption that the nanographite mass density is the same as that of bulk graphite 2.25 g cm^{-3} (Ref. 31). The solid curve in (b) is obtained from the fitting (solid curve) in (a). The E_F vs f_c plot in the case of the absence of the edge state is denoted as the dashed line in (b). The solid curve in (c) is the χ_{orb} at 300 K calculated with the results in (b) based on McClure's theory (Ref. 39). The values for χ_{orb} in (c) are corrected with respect to the systematic experimental error (see text).

associated with the electrostatic forces makes the interior graphene layers less affected by the charge transfer.[38] Therefore the edge states only on the bounding layers are considered to be subjected to the charge transfer, with those on the interior layers remaining around the original Fermi energy.

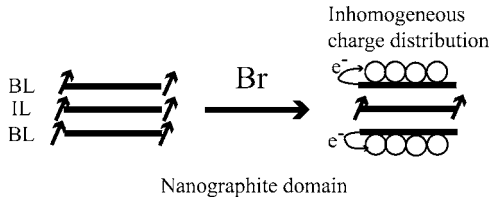

FIG. 14. The schematic description of the inhomogeneous charge transfer between nanographite and bromine. BL and IL denote the bounding layers faced to bromine, and interior layers of nanographite, respectively. The edge-state spins and bromine are schematically shown as the straight arrows and circles, respectively. The edge-state spins disappear on the bounding layers due to the charge transfer.

The CT-independent contribution of the localized spin density is accordingly assigned to the edge-state spins on the interior layers. The contribution of the edge-state spins on the interior layers, which is experimentally estimated as ca. 50% of the total spin density, therefore can be related to the number of the interior nanographene layers. In the meantime, the information on the structure suggests that the mean fraction of the interior nanographene is estimated as 30%–50% of the total number of nanographenes, as each nanographite domain consists of 3 to 4 nanographene layers. Therefore the estimation is in good agreement with the experimental result. Another feature in the discrepancy is that the spin density drop steeper than that calculated in the small f_c region. This can be explained by that only the outer graphene layer can donate the charges to the adsorbed bromine species facing it. Namely, the charge transfer process in the outer graphene layers is responsible for the steep drop.

From the fitting of the observed spin density to Eqs. (4) and (5), the half width and the density-of-states peak height of the edge state are obtained as $W=0.04$ eV, and $D(0)=8\times10^{20}$states eV^{-1} cm^{-3}, respectively. Thus the edge state in the actual nanographite in ACFs is found to have a bandwidth, which ranges around the thermal energy at room temperature.

The CT rate dependence of the Fermi energy is derived using the obtained bandwidth and the density of states peak of the edge state on the basis of Eq. (5). The calculated E_F given in Fig. 13(b) shows a small downshift upon the increase in f_c up to $f_c\sim0.0005$, above which the edge-state spins disappear. Then, the slope of the E_F vs f_c curve becomes steep in the large f_c region. A similar downshift effect of the Fermi energy by the bromine adsorption is also reported in the ESR study for nanographite particles obtained by heat-treatment of nanosized diamond.[15] In the case that the edge state is absent, the Fermi energy is proportional to the square root of f_c due to the contribution of the charge transfer from the linear π-bands as represented in the second term of Eq. (5) and the dotted line in Fig. 13(b). Accordingly, a large deviation of the E_F vs f_c curve from $\sqrt{f_c}$ dependence is the consequence of the contribution of the edge state in the charge transfer process. In other words, it suggests the important role of the edge state in the electronic properties in comparison with the π- and π^*-bands in spite of the fact that the edge-state localized spin density is about several spins per nanographite domain, which corresponds to one spin per 800–1000 carbon atoms involved in a nanographite domain (3 to 4 nanographene layers with the mean in-plane size of 2 to 3 nm).

The orbital susceptibility is also a charge-transfer sensitive parameter. The observed orbital susceptibility shows a steep decrease in its absolute value in the CT rate range up to 0.0001 as shown in Fig. 13(c), where the f_c dependence of χ_{orb} is calculated from a combination of the results in Figs. 4 and 10. In general, the change in the orbital susceptibility is considered to be explained simply in terms of the CT process in graphite.[39] Therefore the change in χ_{orb} can be treated similarly also in the present case on the basis of the CT process. The orbital susceptibility χ_{orb} originates from the interband transition between the π- and π^*-bands in the conjugated π-electron system of nanographite, resulting in its

sensitivity upon the change in the Fermi energy, when the Fermi energy is in the vicinity of the degenerate point. According to McClure's theory, the orbital diamagnetic susceptibility of graphitic systems is given by the following equation:[39]

$$\chi_{\mathrm{orb}}(\mathrm{emu}\ g^{-1}) = -\frac{1.36\times10^{-2}}{T}\ \mathrm{sech}^2\left(\frac{E_{\mathrm{F}}}{2k_{\mathrm{B}}T}\right). \qquad (6)$$

Using the relation between f_c and E_F shown in Fig. 13(b), and Eq. (6), the calculated result for the CT dependence of χ_{orb} is given as a solid line in Fig. 13(c). The calculated χ_{orb} is insensitive to the change in f_c in the small CT region, shows a steep drop around $f_c \sim 0.0005$, and then becomes negligible above that f_c value. Accordingly, there is a large quantitative disagreement between the theory and the experiments; the calculated f_c value at which χ_{orb} shows a steep drop is shifted up to $f_c \sim 0.0005$ in contrast with the experimental behavior showing a steep drop in the initial change of f_c. The energy level broadening of the π-bands might be responsible for the discrepancy between the theoretical estimation and the experimental results for χ_{orb} in nanographite. The presence of the energy level broadening significantly reduces the sensitivity of χ_{orb} to the Fermi energy shift. The inhomogeneous charge distribution, which has been discussed in the behavior of the edge-state spins, induces the inhomogeneous shifts of the Fermi levels with respect to the $\pi-\pi^*$ degenerate point, where only a graphene sheet, whose Fermi level is in the vicinity of the degenerate point, can contribute to the orbital susceptibility. The finite size effect of nanographite works also to reduce the absolute value of the orbital susceptibility to a large extent from that expected for the bulk graphite. In addition, the mixing of the energy level of CT bromine species with the graphitic bands, which will be shown later, can work to modify the feature of the orbital susceptibility.

Here, it is worth discussing the feature of the ESR signal, which is strongly affected by the chemisorbed and CT bromine species. The ESR linewidth steeply increases almost in proportion to the bromine content, and it reaches twice at Br/C=0.23 as large as that of a nonadsorbed sample as shown in Fig. 11. The absolute value of the g-value deviation increases with the increase in the bromine content. These changes in the ESR signal upon bromine uptake is attributed to a large spin-orbital coupling coefficient ($\lambda = 1842\ \mathrm{cm}^{-1}$) of bromine. The observed large g-value deviation and large line broadening upon bromine adsorption suggests the mixing of the energy levels between the nanographite and chemisorbed and charge transfer bromine species. Namely, the edge state and other graphitic bands contain more character of the bromine orbital as the bromine content is elevated.

B. Mechanical and dielectrical effects of physisorbed bromine in nanopores

Next, the effect of the physisorbed bromine species on the electronic properties is discussed. In the typical case of physisorption, almost no electronic effects on host materials are expected because the adsorbed molecules interact with the host only through weak van der Waals interaction. However, recent experiments[19,20] on water adsorption into ACFs have proved that even physisorbed molecules in the nanopore can modify the electronic properties of the host ACFs through a mechanical process due to their soft and flexible structure.

In the water-adsorption process, the water molecules accommodated in the nanopore squeeze nanographite domains, resulting in the reduction in the intergraphene-layer distance in individual nanographite domains.[19] Thus the effective pressure from the guest water molecules enhances the antiferromagnetic exchange interaction between the edge-state spins placed on the adjacent graphene layers through the increase in the wave function overlap, ensuing the reduction in the effective magnetic moment upon the water physisorption. In Br-ACFs, the change in the $\chi_c T$ in Fig. 8 above 230 K can be ascribed to the similar mechanical effect of physisorbed bromine species, taking into account that the melting point of bulk bromine molecules is at 266 K. Because the value of $\chi_c T$ corresponds to the effective spin density, Fig. 8 indicates a gradual decrease in the spin concentration in the temperature region H as the temperature is elevated. The decrease in the effective spin density in the H region is considered to be associated with the enhancement of the antiferromagnetic exchange interaction through the volume expansion of bromine induced by melting of frozen bromine in the nanopore. The density of bromine abruptly drops by ca. 20% at the melting transition from the solid to the liquid phase as shown in Fig. 8(b). The large volume expansion of the guest bromine associated with the density drop works to reduce the internanographene-layers distance in the nanographite domain, resulting in the enhancement in the exchange interaction. In contrast with this, in the freezing process to region M, physisorbed bromine becomes solidified with a release of the chemical pressure induced by volume contraction. Therefore the release of the chemical pressure causes the reduction of the exchange interaction between localized spins. The difference between the bulk melting point 266 K and the temperature, at which the change in the effective magnetic moment ends, can be explained in terms of the size effect on the melting transition and the interaction with nanographite. The condensed phase of physisorbed bromine molecules form nanoclusters in the nanopores, whose size is in the range of ca. 1 to 2 nm. The decrease in the size of the bromine condensed phase and interaction with nanographite can make the melting point considerably reduced, as observed in the experiments.

The change in the effective moment between the intermediate (M) and low temperature ranges (L) also has to be addressed. In the nonadsorbed ACFs, which is the host material for Br-ACFs, the localized spins distribute inhomogeneously with clusterlike structure because they are localized on the edges of nanographene layers, and each nanographite is spatially separated from each other by a nanopore. So the localized spins in the same nanographite domain, which are close to each other, can interact with each other, while the interaction between the spins on different nanographite domains is considered to be weaker than the intradomain interaction. This is evidenced in the observed ESR linewidth in the nonadsorbed ACFs as discussed in the last section. Therefore the larger intradomain interaction works to form short range order of antiferromagnetic spin clusters in the

low temperature region L in spite of the observed paramagnetic behavior, where antiferromagnetic clusters are interacting with each other through the weak interdomain interaction.

Finally, the dielectric effect of the physisorbed bromine species on the electronic transport of the nanographite network is commented. As the experimental observations suggested in the last section, the internanographite domain hopping process is modified upon bromine uptake. Indeed, the electron hopping transport featured with the Coulomb interaction in the nonadsorbed ACFs is changed to the hopping, in which charging energy is less important, in Br-ACFs. According to Eq. (2), the increase in the dielectric constant in the medium between the nanographite domains upon bromine uptake reduces the importance of the charging energy associated with the Coulomb interaction. The accommodation of physisorbed bromine species, which have considerably large dielectrical constant ($\epsilon/\epsilon_0 \sim 3.2$),[42] is responsible for the modification in the charging effect in the electron hopping process.

V. CONCLUSION

The effect of bromine adsorption on the magnetic and electronic properties in a nanographite network system is investigated by using ACFs as a host material. The structure of ACFs consists of a flexible 3D random network of nanographite domains, each of which consists of stacking 3 to 4 nanographene layers. The electronic structure of nanographite is described in terms of a combination of the edge state and the graphitic linear π- and π^*-bands, where the former is located at the degenerate point between the π- and π^*-bands. Adsorption isotherm, TG, and TDS results reveal that the adsorbed bromine species are classified into the three groups with respect to the interaction with nanographite; charge transfer species, covalent bonding species, and physisorption species.

The formation of C–Br covalent bondings takes place through substitution reaction only at the edges of nanographene layers. This suggests that the extension of the graphitic conjugate π-electronic structure remains unchanged by the formation of the covalent bondings due to the inactivity of the carbon atoms in the interior of nanographite in the substitution reaction. However, the mixing of the graphitic and bromine electronic states around the peripheral region of nanographite is found to affect the feature of the edge-states spins.

The CT interaction plays an important role in the electronic properties of nanographite network through the downshift of the Fermi energy. The charge transfer rate dependence of the localized spin density is well explained with the simple electronic structure model consisting of the combination of the linear π- and π^*-bands and edge-state band having a narrow bandwidth comparable to the thermal energy at room temperature. This proves that the edge state plays a role of the electron reservoir in the CT process, resulting in the modification of the behavior of orbital diamagnetism in contrast to the case of a bulk graphite system.

The physisorbed bromine species are accommodated in the nanopore space, and work as effective pressure to the nanographite domains. Squeezing the nanographite domains by the effective pressure reduces the intergraphene-layer distance, resulting in the enhancement in the antiferromagnetic exchange interaction between the edge-state spins on the adjacent nanographene layers. Bromine has a large volume change at the melting transition. Therefore, the bromine liquid phase having a larger specific volume in the nanopore generates higher effective pressure than the solid phase at low temperatures. The melting/freezing transition is found to trigger a low spin/high spin transition in the edge-state spins. This is an unconventional magnetic switching effect of the nanomagnetism in the soft and flexible nanographite network.

ACKNOWLEDGMENTS

The authors are grateful to Professor Kaneko for his suggestion on the measuring of the bromine isotherms for ACFs. Thermogravimetry was carried out at Tamaura and Tsuji Laboratory in T.I.Tech with the support of Dr. Hasegawa. Mass spectroscopy experiments were carried out with the support of Professor T. Komatsu and his students. Raman scattering experiments were performed with the support of Professor K. Iio and his students. The present work was supported by the Grant-in-aid for Scientific Research No. 15105005 and No. 14740378 from Japan Society for Promotion of Science.

*Electronic address: ktakai@chem.titech.ac.jp

[1] *Proceedings of the 5th International Meeting on Small Particles and Inorganic Clusters*, edited by O. Echt and E. Rechnagel (Springer International, Berlin, 1991).

[2] S. Sugano, *Microcluster Physics* (Springer-Verlag, Berlin, 1991).

[3] M. S. Dresselhaus, G. Dresselhaus, and P. C. Eklund, *Science of Fullerenes and Carbon Nanotubes* (Academic Press, San Diego, 1996).

[4] K. Tanaka, S. Yamashita, H. Yamabe, and T. Yamabe, Synth. Met. **17**, 143 (1987).

[5] M. Fujita, K. Wkabayashi, K. Nakada, and K. Kusakabe, J. Phys. Soc. Jpn. **65**, 1920 (1996).

[6] M. Fujita, M. Igami, and K. Nakada, J. Phys. Soc. Jpn. **66**, 1864 (1997).

[7] M. S. Dresselhaus, A. W. P. Fung, A. M. Rao, S. L. di Vittorio, K. Kuriyama, G. Dresselhaus, and M. Endo, Carbon **30**, 1065 (1992).

[8] K. Kaneko, C. Ishii, M. Ruike, and H. Kuwabara, Carbon **30**, 1075 (1992).

[9] A. Nakayama, K. Suzuki, T. Enoki, C. Ishii, K. Kaneko, M. Endo, and N. Shindo, Solid State Commun. **93**, 323 (1995).

[10] N. Kobayashi, T. Enoki, C. Ishii, K. Kaneko, and M. Endo, J.

Chem. Phys. **109**, 88 (1998).
[11] O. E. Andersson, B. L. V. Prasad, H. Sato, T. Enoki, Y. Hishiyama, Y. Kaburagi, M. Yoshikawa, and S. Bandow, Phys. Rev. B **58**, 16387 (1998).
[12] Y. Shibayama, H. Sato, T. Enoki, Xiang-Xin Bi, M. S. Dresselhaus, and M. Endo, J. Phys. Soc. Jpn. **69**, 734 (2000).
[13] Y. Shibayama, H. Sato, T. Enoki, and M. Endo, Phys. Rev. Lett. **84**, 1744 (2000).
[14] K. Takai, H. Sato, T. Enoki, N. Yoshida, F. Okino, Hidekazu Touhara, and M. Endo, J. Phys. Soc. Jpn. **70**, 175 (2001).
[15] B. L. V. Prasad, H. Sato, T. Enoki, Y. Hishiyama, Y. Kaburagi, A. M. Rao, G. U. Sumanasekera, and P. C. Eklund, Phys. Rev. B **64**, 235407 (2001).
[16] K. Oshida, K. Kogiso, K. Matsubayashi, S. Kobayashi, M. Endo, M. S. Dresselhaus, and G. Dresselhaus, J. Mater. Res. **10**, 2507 (1995).
[17] T. Suzuki, K. Kaneko, N. Setoyama, M. Maddox, and K. Gubbins, Carbon **34**, 909 (1996).
[18] T. Suzuki and K. Kaneko, Carbon **26**, 743 (1988).
[19] H. Sato, N. Kawatsu, T. Enoki, M. Endo, R. Kobori, S. Maruyama, and K. Kaneko, Solid State Commun. **125**, 641 (2003).
[20] K. Harigaya and T. Enoki, Chem. Phys. Lett. **351**, 128 (2002).
[21] R. Saito, M. Yagi, T. Kimura, G. Dresselhaus, and M. S. Dresselhaus, J. Phys. Chem. Solids **60**, 715 (1999).
[22] G. H. Findenegg, S. Gross, and T. Michalski, *Fundamentals of Adsorption* (Kodansha, Tokyo, 1992).
[23] N. Kobayashi, Master Thesis, Tokyo Institute of Technology, 1995.
[24] K. Kaneko (private communication).
[25] E. Tanaka, Fuel Combust. **54**, 241 (1987).
[26] Z. Fang, S. Xu, I. S. Butler, R. L. Smith, Jr., and J. A. Koziński, Energy Fuels **18**, 1257 (2004).
[27] K. Kaneko, C. Ishii, N. Nagai, H. Kanoh, Y. Hanzawa, N. Setoyama, and T. Suzuki, Adv. Colloid Interface Sci. **76-77**, 295 (1998).
[28] S. H. Anderson and D. D. L. Chung, Carbon **25**, 191 (1987).
[29] J. B. Pedley, J. Rylance, and Sussex-N. P. L., *Computer Analysed Thermochemical Data: Organic and Organometallic Compounds* (University of Sussex, Brighton, 1977).
[30] J. March, *Advanced Organic Chemistry* (Wiley-Interscience, New York, 1985).
[31] M. S. Dresselhaus, G. Dresselhaus, K. Sugihara, I. L. Spain, and H. A. Goldberg, *Graphite Fibers and Filaments* (Springer-Verlag, Berlin, 1988).
[32] D. S. Knight and W. B. White, J. Mater. Res. **4**, 385 (1989).
[33] L. Pietronero and S. Strässler, Phys. Rev. Lett. **47**, 593 (1981).
[34] C. T. Chan, K. M. Ho, and W. A. Kamitakahara, Phys. Rev. B **36**, 3499 (1987).
[35] M. S. Dresselhaus and G. Dresselhaus, Adv. Phys. **30**, 139 (1981).
[36] B. I. Shklovskii and A. L. Efros, *Electronic Properties of Doped Semiconductors* (Springer-Verlag, Berlin, 1984).
[37] P. R. Wallace, Phys. Rev. **71**, 622 (1947).
[38] S. A. Solin, Mater. Sci. Eng. **31**, 153 (1977).
[39] J. W. McClure, Phys. Rev. **104**, 666 (1956).
[40] E. Ebert, *Landolt-Bŏrnstein, Mechanical-Thermal Properties of States*, 6th ed., II/1 (Springer-Verlag, Berlin, 1971).
[41] L. L. Hawes, Acta Crystallogr. **12**, 34 (1959).
[42] Ch. Wohlfahrt, *Landolt-Bŏrnstein, Static Dielectric Constants of Pure Liquids and Binary Liquids, New Series*, IV/6 (Springer-Verlag, Berlin, 1991).